

Navigation of Untethered Small-Scale Helical Devices Using Magnetic System Under Ultrasound Guidance

Chuang Li¹, Sarthak Misra², *Senior Member, IEEE*, and Islam S. M. Khalil³

Abstract—Magnetic actuation of untethered small-scale helical devices (USHDs) shows great potential for targeted drug delivery or as minimally invasive surgical tools in the human body. However, ensuring the success of therapeutic interventions in anatomically challenging regions, such as neck vascular networks with winding pathways and branching, demands the incorporation of precise image feedback and a robust control method. How to construct a control method with precise navigation ability in complex and hard-to-reach body districts is still a challenging work. In this paper, we propose a closed-loop control strategy for the USHD based on a permanent-magnet robotic (PMR) system inside a three-dimensional (3-D) vascular model with blood. First, the 3-D vascular model is reconstructed using 2-D ultrasound images. Second, the point-to-point closed-loop control of the USHD is performed under ultrasound guidance, and the control input is obtained to act on both the PMR system and the ultrasound system. Next, the USHD navigates the different pathways of the 3-D vascular model under the proposed control strategy. Finally, our *in vitro* experimental results indicate that the maximum mean absolute position error between the target point of each branch and the actual position reached by the USHD (length and diameter of 6 mm and 1.5 mm, respectively) is 6.4 ± 3.8 mm and 4.2 ± 2.8 mm when the blood flow rate is 16.6 mL/min, which corresponds to 28% of the maximum venous flow rate.

Index Terms—Closed-loop control, permanent-magnet robotic system, untethered small-scale helical devices, ultrasound guidance, vascular model.

Manuscript received 18 July 2023; revised 5 September 2023 and 18 September 2023; accepted 19 September 2023. Date of publication 25 September 2023; date of current version 27 October 2023. This article was recommended for publication by Associate Editor V. Iacovacci and Editor P. Dario upon evaluation of the reviewers' comments. This work was supported in part by the European Research Council (ERC) through the European Union's Horizon 2020 Research and Innovation Programme under Grant 866494 (Project-MAESTRO), and in part by the China Scholarship Council (CSC). (Corresponding author: Chuang Li.)

Chuang Li is with the Surgical Robotics Laboratory, Department of Biomedical Engineering, University of Groningen and University Medical Centre Groningen, 9713 GZ Groningen, The Netherlands (e-mail: c.li01@umcg.nl).

Sarthak Misra is with the Surgical Robotics Laboratory, Department of Biomedical Engineering, University of Groningen and University Medical Centre Groningen, 9713 GZ Groningen, The Netherlands, and also with the Surgical Robotics Laboratory, Department of Biomechanical Engineering, University of Twente, 7500 AE Enschede, The Netherlands (e-mail: s.misra@umcg.nl).

Islam S. M. Khalil is with the Surgical Robotics Laboratory, Department of Biomechanical Engineering, University of Twente, 7500 AE Enschede, The Netherlands (e-mail: i.s.m.khalil@utwente.nl).

This article has supplementary downloadable material available at <https://doi.org/10.1109/TMRB.2023.3318642>, provided by the authors.

Digital Object Identifier 10.1109/TMRB.2023.3318642

I. INTRODUCTION

VASCULAR diseases are highly prevalent conditions, such as strokes and arteriosclerosis, which pose significant threats to human health [1]. Current treatments for vascular diseases, including drug therapy, vascular bypass graft, and carotid angioplasty, have adverse effects such as invasiveness, and potential complications [2], [3], [4], [5]. To overcome the limitations of current treatments for vascular diseases, innovative devices such as untethered small-scale helical devices (USHDs) have been developed [6], [7], [8]. These miniature devices have potential impact in targeted and minimally invasive interventions, enabling precise navigation through intricate vascular networks and providing more effective and safer treatment than traditional methods [9], [10]. One promising approach to achieving the capabilities mentioned above is through the use of magnetically-driven USHDs [11]. By an externally applied rotating magnetic field, these USHDs can be controlled and guided inside the blood vessels, enabling them to navigate with high precision and maneuverability [12], [13]. The use of magnetism as a magnetic force or torque eliminates the need for tethers or external wires, allowing for minimally invasive procedures and reducing the risk of complications [14].

Recently, several studies have explored the potential of magnetic control of the USHD in various medical applications. For instance, Mahoney and Abbott have showcased a method to generate a rotating magnetic field with any desired rotation axis using a single rotating magnet actuator to actuate a magnetic device [15]. They have also presented the kinematic model of a magnetic microrobot swarm operating within a single rotating magnetic field [16]. This model provides valuable insights into the motion state of the microrobot swarm, allowing us to better understand its collective behavior. In addition, Alshafei et al. have proposed a method by using synchronously rotating two permanent magnets to control a helical robot in a glass tube, resulting in the establishment of a relationship between the movement speed of the helical robot and the rotation frequency of the permanent magnet [17]. Furthermore, Mahdy et al. have utilized a helical robot to verify its characteristics of helical propulsion inside *in vitro* and *ex vivo* models of a rabbit aorta [18]. Moreover, Tan and Cappelleri have proposed a novel fabrication method to enhance the swimming performance of helical robots by leveraging the benefits of a robust magnetic head and a flexible deformable tail [19].

Liu et al. have proposed a closed-loop sliding mode control method by using electromagnetic actuation and visual feedback to enable the miniature helical swimmer to track the corresponding path and avoid obstacles, thereby improving the robustness of the entire system [20]. For the application of helical robots in medical treatment, Khalil et al. have proposed the use of a helical robot to clear blood clots and established the corresponding mathematical model and further used *in vitro* verification [21]. This research group has employed the helical robot to clear blood clots under ultrasound guidance [22]. Leclerc et al. also have proposed a control apparatus [23] to perform three-dimensional (3-D) path following and clear blood clots by using a miniature magnetic swimmer [24].

Although the above works have proposed many advanced methods and equipment, there is still room for improvement. For instance, the only basic screw characteristics of helical propulsion of the robot under two synchronously rotating permanent magnets have been studied [17], [18]. Furthermore, the researcher only has studied the 1-D motion of the helical robot and implemented a clear experiment of thrombus [21], [22]. Despite some previous work successfully showcasing the movement of helical robots along simplified 3-D paths and their related applications, these paths do not capture the geometry of the blood vessels. Hence, the vascular models that accurately represent anatomical structures should be considered. Moreover, to achieve precise navigation of USHDs inside blood vessels, the reconstruction of complex 3-D vascular geometry is an indispensable foundational element. In this context, ultrasound stands as the preferred imaging modality due to its non-invasive nature, ease of operation, and cost-effectiveness. Yang et al. have used an ultrasound system to scan cross-sectional views of the vascular model [25]. By utilizing the positional information obtained from the ultrasound probe and the 2-D ultrasound images, they have successfully derived the centerline of the 3-D vascular model. Yang et al. have also utilized an ultrasound system to scan the vascular model, thereby obtaining 2-D ultrasound images [26]. Subsequently, speckle noise within the subsequent ultrasound images has been removed using blur, dilation, and erosion filters, and then the 3-D point cloud of the vascular model has been generated by integrating the position of the ultrasound probe. De Ruijter et al. have developed a general, robust, and accurate approach for segmenting the lumen-wall boundary of both healthy central and peripheral vessels within extensive field-of-view freehand ultrasound datasets [27]. This has been achieved by employing Convolutional Neural Networks, subsequently leading to the reconstruction of the vascular geometry. Taking inspiration from these works, we also employ an ultrasound system to reconstruct the 3-D vascular models, subsequently obtaining reference paths for the navigation of the USHD. In addition, performing minimally invasive surgery inside complex vascular networks requires a certain amount of space to ensure precision and effectiveness. Therefore, there is a need for advanced control strategies and devices that can navigate the complex and irregular paths of blood vessel networks, while

providing sufficient working space for minimally invasive procedures.

In this paper, we investigate the movement of a USHD inside the 3-D vascular model using a permanent-magnet robotic (PMR) system guided by the ultrasound system, as shown in Fig. 1. In our experiments, the construction of a closed-loop feedback control system allows for real-time adjustments of the PMR system based on medical ultrasound images and predefined paths. This ensures that the USHD can accurately follow a predetermined trajectory inside the 3-D vascular model, minimizing the risk of deviation from the intended path. Compared to manual navigation of the USHD by interventional physicians, the use of the PMR system has the potential to provide more stable and consistent control for the USHD's movements, reducing the potential for errors caused by human factors such as fatigue or hand tremors. In addition, the use of a feedback control robotic approach also has the potential to reduce the burden on the interventionalist or radiologist while ensuring guidance precision. The main contributions of this paper are as follows:

(a) The integration of a mobile ultrasound imaging device with the PMR system allows for simultaneous localization and control of the USHD. This integration enhances the precision and accuracy of the navigation process by providing real-time imaging feedback.

(b) A control method with robustness is constructed using the PMR system and the reconstructed 3-D vascular model based on 2-D ultrasound images, and the proposed approach is able to drive the USHD through complex and winding paths inside the 3-D vascular model.

(c) The research evaluates the locomotion performance of the USHD inside the 3-D vascular model under various blood flow velocities. This assessment provides insights into how the USHD behaves in different flow conditions, contributing to the understanding of the capabilities and limitations of the control method proposed.

The remainder of this paper is organized as follows: The blood flow field is analyzed and the 3-D vascular model is reconstructed in Section II. The PMR system is described, and the closed-loop control method of the USHD inside the 3-D vascular model is presented and experimental results are analyzed in Section III. Section IV provides discussions pertaining to the limitations and potential applications of the USHDs. Finally, Section V concludes and provides directions for future work.

II. 3-D VASCULAR MODEL

The 3-D vascular model used in the experiment is described, as shown in Fig. 1(B). Two paths are planned in the 3-D vascular model. The first path is from starting point to target point 1 in path 1, the other path is from target point 1 to target 2. Our objective is to guide the USHD through path toward the target position. During the motion control experiment of the USHD, chicken tissue is used to cover the surface of the 3-D vascular model and the direction of blood flow in the 3-D vascular model is from right to left, as shown in Fig. 2(A).

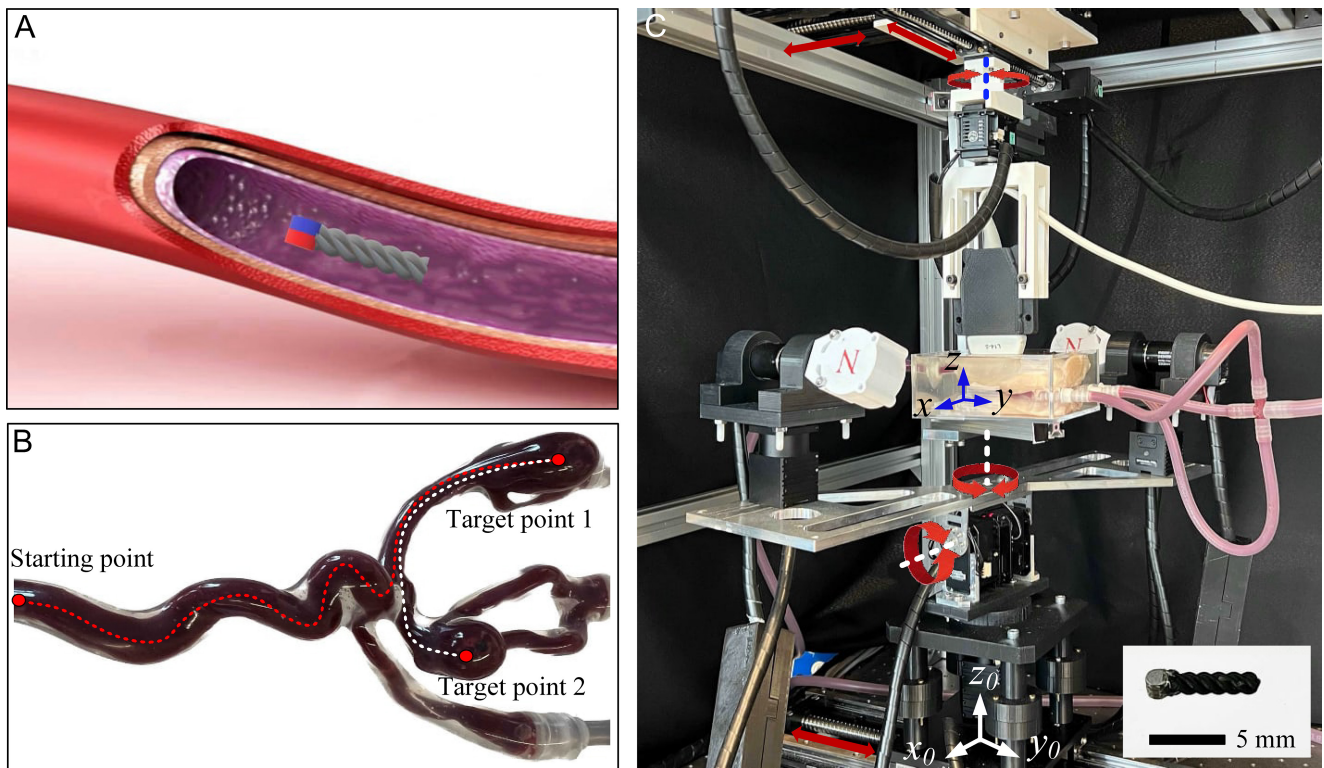


Fig. 1. A permanent-magnet robotic (PMR) system for an untethered small-scale helical device (USHD) inside a 3-D vascular model. (A) The USHD is actuated inside the 3-D vascular model. (B) Two paths are planned in the 3-D vascular model, where the first path is from the starting point to the target point 1, and the second path is from the target point 1 to the target point 2. (C) The PMR system is used to actuate the USHD toward the target position in the 3-D vascular model, where 3-DOF (pitch, yaw, and a linear motion stage) are used to control the position of two synchronously rotating permanent magnets fixed to two DC motors, and other 3-DOF (rotation and two linear motion stages) can control the position of the ultrasound probe in the global coordinate system $\{x_0, y_0, z_0\}$. The 3-D vascular model is fixed in the container and the phantom frame is indicated by $\{x, y, z\}$.

A. Characterization of the Flow Field Inside the 3-D Vascular Model

In medical applications, Color-flow Doppler mode can be used to calculate the velocity of the fluid within the target area by measuring the Doppler frequency shift [28]. Therefore, we characterize the pulsatile blood flow field based on Doppler ultrasound imaging. The blood flow velocity varies throughout the vascular model. It typically follows a parabolic profile [29], with the highest velocity occurring at the center of the vessels and gradually decreasing towards the vessel walls, as shown in Fig. 2(C,D,E). In the 3-D vascular model, when the blood flow velocity is low, it is usually in a state of laminar flow, and the Reynolds number $Re = \frac{\rho_f |v_b| L}{\mu}$ ($O(10^{-1})$) is small at this time, where ρ_f is the density of the blood, v_b is the blood flow velocity, and μ is the viscosity of the blood, and L is the characteristic length. In the laminar flow state, the blood flow is relatively stable, the streamlines are arranged in an orderly manner, and there is no obvious disorder or turbulence [30]. In this case, the Reynolds number is small, the inertial effect of the blood is relatively small, and the viscous force plays a dominant role. However, when blood flow velocity increases, a transition may occur in the vascular model, from a laminar to a turbulent state of flow. In the turbulent state, the streamlines are chaotic and randomly arranged, and there are eddies and turbulent eddies. At this time, the Reynolds number becomes

larger, and the inertial effect of the blood begins to be significant, playing a leading role in the flow. In actual human veins, the blood flow is usually in a state of laminar flow [31], due to the relatively large diameter of the vein and the relatively slow speed of blood flow. It should be noted that venous blood flow may also be turbulent in certain situations, such as in narrowed veins or at the confluence of vascular branches or when disturbed by external pressure. This turbulent state can lead to non-uniform blood flow velocity, increased vortices and mixing phenomena, exerting additional pressure and shear forces on the vein wall.

In addition, the Reynolds number is inversely proportional to blood viscosity. When the blood viscosity increases, the Reynolds number decreases if other parameters remain constant. This is because higher viscosity increases the resistance of blood, causing a change in the balance of inertial and viscous forces during flow [32]. From Fig. 3, we can obtain that the blood viscosity decreases with the shear rate. Therefore, when the USHD swims through blood vessels at different rotational frequencies, it also changes the viscosity of the surrounding blood. Furthermore, variations in the velocity and viscosity of blood flow cause constant changes in resistance to the USHD, which can have implications for the USHD's stability, control, and navigation. Therefore a robust control method should be considered.

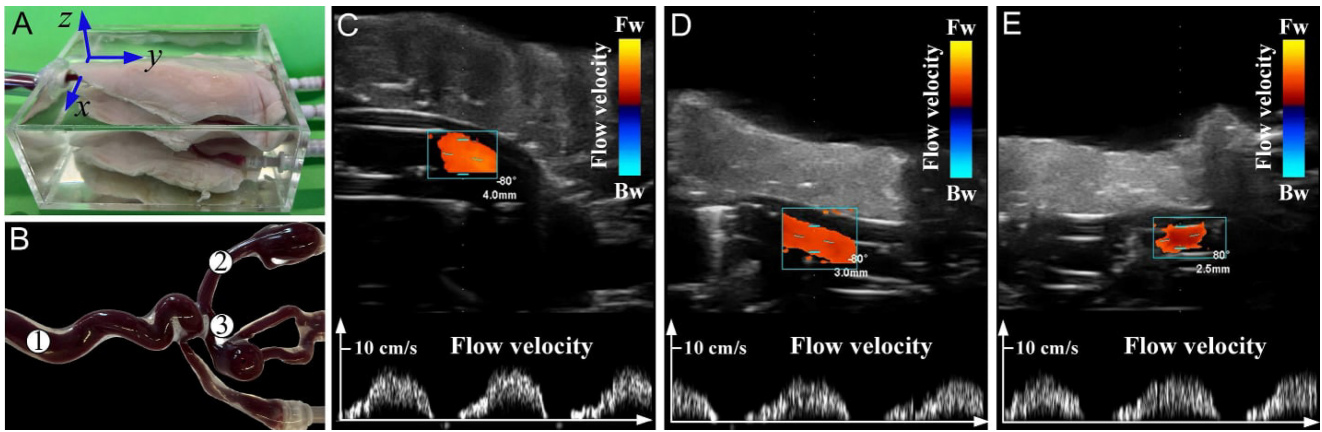


Fig. 2. Blood flow field analysis inside the 3-D vascular model. (A) Chicken tissue covers the 3-D vascular model during closed-loop control of the USHD. (B) Ultrasound Doppler mode is used to measure blood flow velocity at locations ①, ②, and ③ when the flow rate of 33.3 mL/min is provided to the 3-D vascular model. (C) The blood velocity at position ① is measured. (D) The blood velocity at position ② is measured. (E) The blood velocity at position ③ is measured. Fw, forward; Bw, backward.

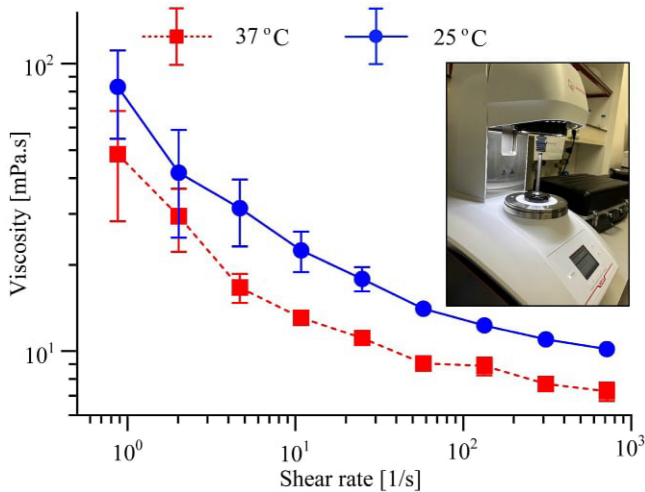


Fig. 3. The mechanical properties of the blood are characterized using a rheometer. The viscosity of blood is measured at room temperature (25°C) and body temperature (37°C), respectively.

B. Ultrasound Volume Reconstruction of the 3-D Vascular Model

As shown in Fig. 4(A), this is a regular *in vitro* model of the 3-D vascular network which is fixed in a transparent container with a length, width, and height of 140 mm, 120 mm, and 50 mm. We define the width, length, and height of the container as the axis of the *in vitro* model coordinate system $\{x, y, z\}$. Additionally, the 3-D vascular model is a real-sized, silicone vascular model that replicates a particular neck anatomy, and target points 1 and 2 (Fig. 1(B)) are two angiomas. Before the motion control of the USHD inside the 3-D vascular model, the environment reconstruction of the 3-D vascular model is critical to plan the navigation path of the USHD. In the reconstruction process, the probe of the ultrasound system is automatically controlled to scan the 3-D vascular model along the y_0 -axis in the global coordinate system, and equal interval ultrasound images are obtained. Further, these ultrasound images are processed to reconstruct the 3-D vascular model. A region of interest (ROI) is selected (Fig. 4(B)) so that the high region and the lower region with

a strong reflection of the ultrasound image are cropped. Then, the speckle noise is removed by using Gaussian blur, we binarize the gradient on the ultrasound image and extract the edges of the image, and then extract the corresponding points, as shown in Fig. 4(B). The 3-D point cloud can be obtained by combining the position of the ultrasound probe and corresponding 2-D ultrasound images, and the waypoints are further extracted by image processing in each slice, as shown in Fig. 4(C). Therefore, the coordinates $\{\xi_v\}$ of the 3-D vascular model can be obtained as follows:

$$\xi_v = \begin{bmatrix} q_1 - x_o - l_p(p_c - p_x) \\ q_2 - y_o \\ h_p - l_p p_y \end{bmatrix}^T, \quad (1)$$

where q_1 and q_2 are the positions of ultrasound probe along the x_0 -axis and y_0 -axis directions. x_o and y_o are the position of the origin of the vascular model coordinate system in the x_0 -axis and y_0 -axis directions of the global coordinate system. p_x and p_y denote the coordinates of each point after extraction in the 2-D ultrasound image plane, and p_c represents the midpoint pixel coordinate in the horizontal direction of the 2-D ultrasound image plane. h_p represents the vertical distance from the ultrasound probe to the xy -plane. l_p represents the size of each pixel. This procedure is performed during the preoperative stage, and the generated path will serve as a reference for motion control of the USHD inside the 3-D vascular model.

For the objective assessment of ultrasound-based reconstruction of the 3-D vascular model, manually labeled ground-truth is used. In accordance with our methodology for the vascular model reconstruction, an analysis of cross-sectional 2-D ultrasound images of the vascular model leads to the computation of the Dice Coefficient, yielding a value of 0.905 ± 0.037 . Furthermore, the Euclidean distance between corresponding points within the two point clouds is determined to be 2.388 ± 0.623 mm. Additionally, from the reconstructed 3-D vascular model, it is observed that path 1 exhibits a greater curvature compared to path 2. The maximum curvature along path 1 is measured at 19.6 mm^{-1} , while path 2 reaches a maximum curvature of 1.9 mm^{-1} . The degree of curvature of the vascular model will impact the control of the USHD

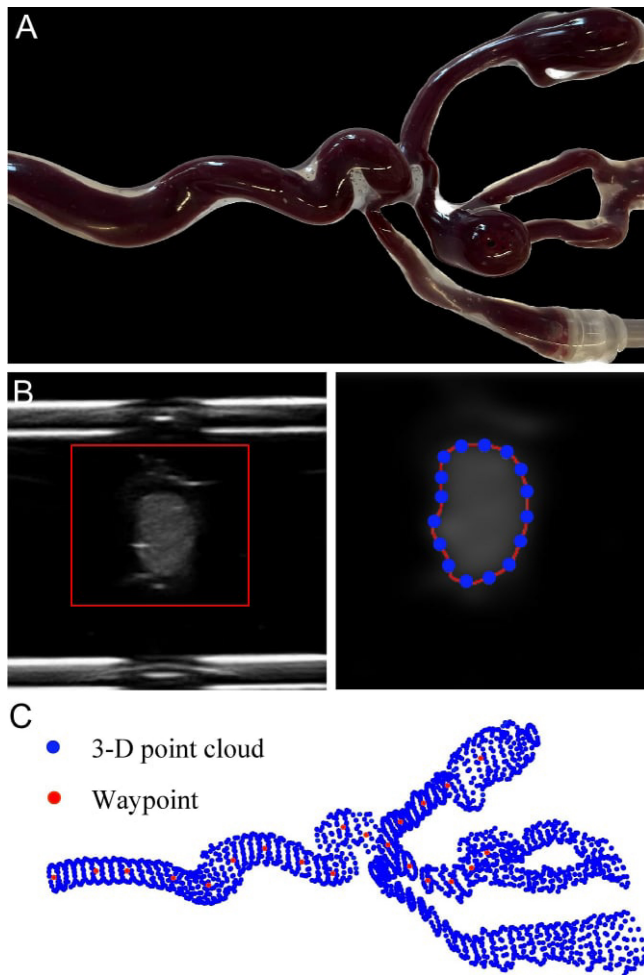


Fig. 4. The environment reconstruction of the 3-D vascular model based on the ultrasound imaging system. (A) A 3-D vascular model is scanned by the ultrasound system. (B) The ultrasound B-mode obtains equal interval ultrasound images, and a region of interest (ROI) is extracted in the origin ultrasound image. The Gaussian blur is applied to the ultrasound image. After applying the Gaussian blur, the adaptive thresholding technique is used on the ROI. Following the adaptive thresholding step, edge extraction is performed on the ROI of the ultrasound image. (C) Based on the 2-D ultrasound images and the position of the ultrasound probe, the 3-D vascular model is reconstructed using the 3-D point cloud.

during the closed-loop control experiments. Note that in the process of ultrasound guiding the USHD, the selection of the dynamic ROI of the 3-D vascular model is also based on the reconstructed vascular model.

III. MOTION CONTROL OF THE USHD

The PMR system of 6-DOF is used to guide a USHD inside the 3-D vascular model. Two DC motors are used to rotate the permanent magnets to generate the rotating magnetic field and the axis of the rotating magnetic field is controlled to guide the USHD inside 3-D vascular model, as shown in Fig. 1(C).

A. System Description

In the PMR system, there are 6-DOF, three of which are utilized to adjust the position of the transducer (SonixTouch Q+, BK Medical, Quickborn, Germany). The motion of the ultrasound probe along the x_0 -axis, the motion along the y_0 -axis,

TABLE I
SPECIFICATION OF THE UNTETHERED SMALL-SCALE HELICAL DEVICE (USHD) AND A PERMANENT-MAGNET ROBOTIC (PMR) SYSTEM. d_t AND l_t ARE THE DIAMETER AND LENGTH OF THE USHD, RESPECTIVELY. $\mathbf{M}_{1,2}$ AND \mathbf{m} ARE MAGNETIC DIPOLE MOMENTS OF TWO ROTATING PERMANENT MAGNETS AND THE USHD. ρ_f IS THE DENSITY OF THE BLOOD, AND R_e IS REYNOLDS NUMBER. f_r IS FREQUENCY OF ULTRASOUND WAVES, AND G_n IS GAIN OF ULTRASOUND SYSTEM. TIS IS THE THERMAL INDEX SCORE, AND MI IS THE MECHANICAL INDEX

Parameter	Value	Parameter	Value
d_t [mm]	1.5	l_t [mm]	6
Pitch [mm]	1	Helicity [$^\circ$]	71
$M_{1,2}$ [A.m ²]	52.26	\mathbf{m} [A.m ²]	6.23×10^{-4}
ρ_f [kg/m ³]	1050	R_e	O(10^{-1});O(10)
f_r [MHz]	14	G_n	42
TIS	0.21	MI	0.72

and its own rotational motion are denoted as q_1 , q_2 , and q_3 , respectively. The remaining 3-DOF are employed to control the pitch, motion along the y_0 -axis of the rotating magnetic field, and yaw denoted as q_4 , q_5 , and q_6 . These 6-DOF are controlled by six servo motors (MX-106R Dynamixel, Robotis, South Korea) respectively, as shown in Fig. 1(C). Two permanent magnets (NdFeB, R750F, Amazing Magnetic LLC, California, U.S.A) with diameter and height of 40 mm and 35 mm, are respectively installed on two DC motors (Maxon 47.022.022-0019-189 DC Motor Maxon Motors, Sachseln, Switzerland), which has a magnetization of 1.72×10^{-4} A.m², and the distance between the two permanent magnets is 35 cm. The field strength at the midpoint of the two magnets is approximately 5 mT. The orientation and location of the two DC motors are controlled independently using q_4 , q_5 , and q_6 to change the pitch and yaw angles of the USHD in different locations. The USHD (Fig. 1(C)) with length of 6 mm and diameter of 1.5 mm is fabricated through 3-D printing using polylactic acid filament (PrimaValue, 3-D Printers, The Netherlands). A cylindrical NdFeB magnet with diameter of 1.5 mm and length of 1.5 mm is attached to the USHD. In addition, a pulsation pump (HV-77910-55, Masterflex, Illinois, U.S.A) is used to provide blood flow at different flow rates into the anatomical vascular model (HN-S-A-006, Neck model, Elastrat, Switzerland). In our experiments, pig blood is used and a rheometer (MCR 92, Modular Compact Rheometer, Anton Paar, Austria) is used to measure the viscosity of the blood at room temperature and body temperature, respectively. The 3-D vascular model is covered by chicken breast tissue, and demineralized water is poured into the container so that there are no gaps between the 3-D vascular model and the tissues, as shown in Fig. 2(A). Specifications of the USHD and the PMR system are described in Table I.

B. Control Strategy

We propose a point-to-point closed-loop control method that ensures the USHD reaches the predetermined target position under ultrasound imaging guidance. The navigation strategy consists of two key steps: the USHD recognition and the rotating magnetic field direction adjustment.

1) *Identification and Tracking of the USHD*: During the USHD movement, the ultrasound probe needs to be moved according to the position of the reconstructed 3-D vascular model and the position of the USHD. Therefore, before the closed-loop control of the USHD, we need to predefine the position of the ultrasound probe based on the reconstructed 3-D vascular model using q_1 , q_2 , and q_3 .

$$\frac{q_1 - x_j}{q_2 - y_j} = \frac{q_1 - x_{j+1}}{q_2 - y_{j+1}}, \quad (2)$$

where $\mathbf{p}_j = (x_j, y_j, z_j)^T \in \mathfrak{R}^{n \times 3}$ is the waypoint of the 3-D vascular model in the global coordinate frame. Furthermore, q_3 can be defined using

$$q_3 = \tan^{-1} \left(\frac{x_{j+1} - x_j}{y_{j+1} - y_j} \right). \quad (3)$$

In order to ensure that the imaging of the vascular model is within the 2-D ultrasound plane, q_1 and q_2 need to be constrained using

$$\begin{cases} \sqrt{(q_1 - x_j)^2 + (q_2 - y_j)^2} \leq \frac{l_u}{2} \\ \sqrt{(q_1 - x_{j+1})^2 + (q_2 - y_{j+1})^2} \leq \frac{l_u}{2} \end{cases}, \quad (4)$$

where l_u is the width of the ultrasound image. Hence, q_1 , q_2 , and q_3 can be predefined before the closed-loop control experiment of the USHD. In order to achieve accurate control of the USHD, the recognition of the USHD in 2-D ultrasound images is crucial. Since the chicken breast tissue covers the 3-D vascular model in our experiment, it would bring noise to the ultrasound image. To reduce the effect of image noise, dynamic ROIs are selected based on the reconstructed model and the position of the ultrasound probe. Further, we binarize the ROI, the USHD is detected due to the different reflections of ultrasonic sound waves between the USHD and blood. Therefore, based on the position of the ultrasound probe and the position of the USHD in the ultrasound image, the position (\mathbf{p}_g) of the USHD in the global coordinate frame can be obtained using

$$\mathbf{p}_g = \begin{bmatrix} q_1 - (p_c - u)l_p \sin q_3 \\ q_2 - (p_c - u)l_p \cos q_3 \\ h_g - l_p v \end{bmatrix}, \quad (5)$$

where u and v represent the pixel coordinates of the USHD's position in the 2-D ultrasound image, and h_g represents the vertical distance from the ultrasound probe to the x_0y_0 -plane.

2) *Construction of an Ideal Rotating Magnetic Field*: The two synchronously rotating permanent magnets are used to control the USHD in the 3-D vascular model, and the rotation axis of the permanent magnet is adjusted to construct the ideal rotating magnetic field. In the PMR system, each field is modeled according to the following point-dipole approximation [33], [34]:

$$\mathbf{B}_i(\mathbf{p}) = \frac{\mu_0}{4\pi|\mathbf{p}|^3} \left(\frac{3(\mathbf{M}_i \cdot \mathbf{p})\mathbf{p}}{|\mathbf{p}|^2} - \mathbf{M}_i \right) \quad i = 1, 2, \quad (6)$$

where \mathbf{B}_1 and \mathbf{B}_2 respectively represent the magnetic field generated by two permanent magnets, μ_0 represents the penetration constant, and \mathbf{p} is the position vector of the USHD

with respect to the rotating permanent magnet, and \mathbf{p} can be calculated using the position (\mathbf{p}_g) of the USHD in the global coordinate frame. \mathbf{M}_i denotes the magnetic dipole moment of i th permanent magnet. We assume that enough torque is provided using the external rotating magnetic field, and the magnetization of the USHD ultimately aligns with the magnetic field lines. Consequently, the motion direction of the USHD can be changed using the direction of the external driving magnetic field at the position of the USHD.

According to the point-dipole approximation model (6) and the direction error of the USHD in the 3-D vascular model, the angles of the ideal rotating magnetic field can be obtained using

$$\angle \mathbf{B}_p(\mathbf{p}) = \tan^{-1} \left(\frac{\sqrt{(\mathbf{p}_i - \mathbf{p})_x^2 + (\mathbf{p}_i - \mathbf{p})_y^2}}{(\mathbf{p}_i - \mathbf{p})_z} \right), \quad (7)$$

where $\angle \mathbf{B}_p(\mathbf{p})$ represents the ideal angles of the rotating magnetic field in the pitch direction, and \mathbf{p}_i is the waypoint with respect to the rotating permanent magnet. Furthermore, we can calculate the ideal angles of the rotating magnetic field in yaw direction using

$$\angle \mathbf{B}_y(\mathbf{p}) = \tan^{-1} \left(\frac{(\mathbf{p}_i - \mathbf{p})_x}{(\mathbf{p}_i - \mathbf{p})_y} \right). \quad (8)$$

Therefore, we can obtain desired magnetic field $\mathbf{B}^d(\mathbf{p})$ based on the angle ($\angle \mathbf{B}_p(\mathbf{p})$ and $\angle \mathbf{B}_y(\mathbf{p})$) of the desired magnetic field, and then calculate the desired magnetization \mathbf{M}^d using Equation (6) [8]. Then an ideal rotating magnetic field can be constructed by changing joint space coordinates (q_4, q_5, q_6). In addition, a proportional-integral-derivative controller $\omega = k_p|\mathbf{e}| + k_i \int_0^t |\mathbf{e}|dt + k_d|\dot{\mathbf{e}}|$ is used to control the rotation angular frequency of the magnetic field, where $|\mathbf{e}| = |\mathbf{p}_i - \mathbf{p}|$ is the position error, and k_p , k_i , and k_d all non-negative, denote the coefficients for the proportional, integral, and derivative terms respectively. Note that the selection of these coefficients depends on the velocity of the blood flow and the geometry of the 3-D vascular model. Further, the rotation frequency of the magnetic field is less than the step-out frequency. Finally, we implement an OpenCV (version 3.4.9) image processing library to detect and track the USHD in the ultrasound system frame. The control strategy is implemented in C++ on a computer running Linux Ubuntu 16.04. A pseudocode of the closed-loop control implementation is provided in Table II.

C. Experimental Results

The USHD is controlled to swim toward the target point inside the 3-D vascular model under the proposed control strategy. During the closed-loop control experiments of the USHD, the ultrasound B-mode is applied to obtain ultrasound images at frame rate of 28 Hz, and the different blood flow rates are provided in the 3-D vascular model.

TABLE II
PSEUDOCODE OF THE CLOSED-LOOP CONTROL OF THE USHD INSIDE
THE 3-D VASCULAR MODEL USING THE PMR SYSTEM AND
ULTRASOUND GUIDANCE

Algorithm: Control algorithm for the USHD

Input:
waypoint group $\mathbf{p}_i \in \mathbb{R}^{n \times 3}$;
position of the ultrasound probe $\mathbf{p}_b = (q_1, q_2, q_3)^T \in \mathbb{R}^{j \times 3}$;
ROI of the 3-D vascular model;
real-time 2-D ultrasound images $\mathbf{U}_f \in \mathbb{R}^{u \times v}$;
error thresholds ε ;

Output:
position \mathbf{p} of the USHD;
input of the PMR system (q_1 - q_6);
angular frequency of the rotating magnetic field ω ;

Initialization:
 $i:=1$, $b:=1$, and $(q_1(0) - q_6(0))$;

while $i \leq n$ **do**
 $|\mathbf{e}| = |\mathbf{p}_i - \mathbf{p}|$;
 $\omega = k_p |\mathbf{e}| + k_i \int_0^t |\mathbf{e}| dt + k_d |\dot{\mathbf{e}}|$;
if $|\mathbf{e}| < \varepsilon$;
 $i \leftarrow i + 1$;
 $b \leftarrow b + 1$;
 $\angle \mathbf{B}_p(\mathbf{p}) = \tan^{-1} \left(\frac{\sqrt{(\mathbf{p}_i - \mathbf{p})_x^2 + (\mathbf{p}_i - \mathbf{p})_y^2}}{(\mathbf{p}_i - \mathbf{p})_z} \right)$;
 $\angle \mathbf{B}_y(\mathbf{p}) = \tan^{-1} \left(\frac{(\mathbf{p}_i - \mathbf{p})_x}{(\mathbf{p}_i - \mathbf{p})_y} \right)$;
 $\mathbf{B}^d(\mathbf{p}) \leftarrow \angle \mathbf{B}_p(\mathbf{p})$ and $\angle \mathbf{B}_y(\mathbf{p})$;
 $\mathbf{M}^d \leftarrow \mathbf{B}^d(\mathbf{p})$;
 $(q_4, q_5, q_6) \leftarrow \mathbf{M}^d$;
end

end

We first perform navigation experiments of the USHD inside the 3-D vascular model encased in chicken tissue. In path 1 (Fig. 1(B)) of the 3-D vascular model, the USHD swims from starting point toward target point 1, as shown in Fig. 5. During the motion control of the USHD in path 1, the joint space coordinate of the PMR system can be obtained ($n = 5$) under the proposed control method, when the blood flow rates are 0 mL/min, 16.6 mL/min, and 33.3 mL/min, as shown in Fig. 5(A). q_1 , q_2 , and q_3 are updated based on the reconstructed 3-D vascular model and the current position of the USHD, and q_4 , q_5 , and q_6 can be calculated based on the current position of the USHD and the position of the waypoints in path 1 under the proposed control strategy. For path 1, the angle of the rotating magnetic field and the position of the ultrasound probe can be changed using the joint space coordinate (q_1 - q_6) of the PMR system, when the blood flow rate is 16.6 mL/min, as shown in Fig. 5(B). Furthermore, five ultrasound tracking instants are shown in Fig. 5(C), demonstrating that, although there is noise in the ultrasound image due to the wrapping of chicken tissue and the vascular model wall, the USHD can be identified and tracked stably under our

proposed method. Fig. 5(D) plots the USHD navigation results and shows the position of the USHD and centerline of path 1 of the 3-D vascular model ($n = 5$) when the flow rate of blood is 16.6 mL/min. *Please refer to the accompanying video.*

Similar to path 1, the USHD swims toward target point 2 along path 2 of the 3-D vascular model, as shown in Fig. 6. Fig. 6(A) demonstrates the control input obtained for path 2 ($n = 5$) when flow rates of 0 mL/min, 16.6 mL/min, and 33.3 mL/min are provided in the 3-D vascular model. Fig. 6(B) illustrates five instances of the PMR system configurations when the blood flow rate is 16.6 mL/min, while Fig. 6(C) displays the corresponding five instances of ultrasound tracking along path 2 at these instances. The motion trajectories of the USHD inside path 2 of the 3-D vascular model are extracted ($n = 5$), as shown in Fig. 6(D). By examining the control inputs (q_1 - q_6) depicted in Fig. 5(A) and Fig. 6(A) for paths 1 and 2 respectively, we observe that the control inputs remain similar across the 5 trials, indicating the stable performance of the PMR system and the effectiveness of the proposed control method. *Please refer to the accompanying video.*

In order to further evaluate the stability performance of the PMR system, we continue to repeat closed-loop control experiments of the USHD at blood flow rates of 0 mL/min, 16.6 mL/min, and 33.3 mL/min respectively, where the blood flow rate of 33.3 mL/min corresponds to 56% of the maximum venous flow rate [35]. For each path and each blood flow rate, we perform 30 consecutive trials ($n = 30$). From experiments, we observed that when the flow rate is 0 mL/min, regardless of path 1 or path 2, the success rate of the USHD reaching the target point is extremely high under our proposed control method, as shown in Fig. 7(A). In this case, the success rate of path 1 is slightly lower than that of path 2 due to the higher curvature of path 1. However, when the blood flow rate increases, the success rate of the USHD for paths 1 and 2 to the target position decreases, because the pulsating blood flow (Fig. 2(C,D,E)) brings external disturbances in the motion control of the USHD. In the presence of blood flow, the success rate of path 2 is lower than that of path 1. This outcome can be attributed to the intersection of path 1 and path 2. Due to the influence of blood flow, the USHD might mistakenly enter path 1 instead of swimming towards the intended target point 2, and the USHD enters the wrong vascular model branch and then loses the target, which leads to the failure of the USHD's navigation. From the experimental results, it can be seen that when the blood flow rate is 16.6 mL/min, the success rate of the PMR system controlling the USHD in the 3-D vascular model is higher than 75%. Further, in the experimental trials with successful navigation, we calculated that as the blood flow rate increases, the mean absolute error of the USHD reaching the target position increases under our proposed control method, as shown in Fig. 7(B). In addition, the target position in path 1 exhibits a steeper inclination compared to the target position in path 2, resulting in a greater mean absolute error of the USHD in path 1.

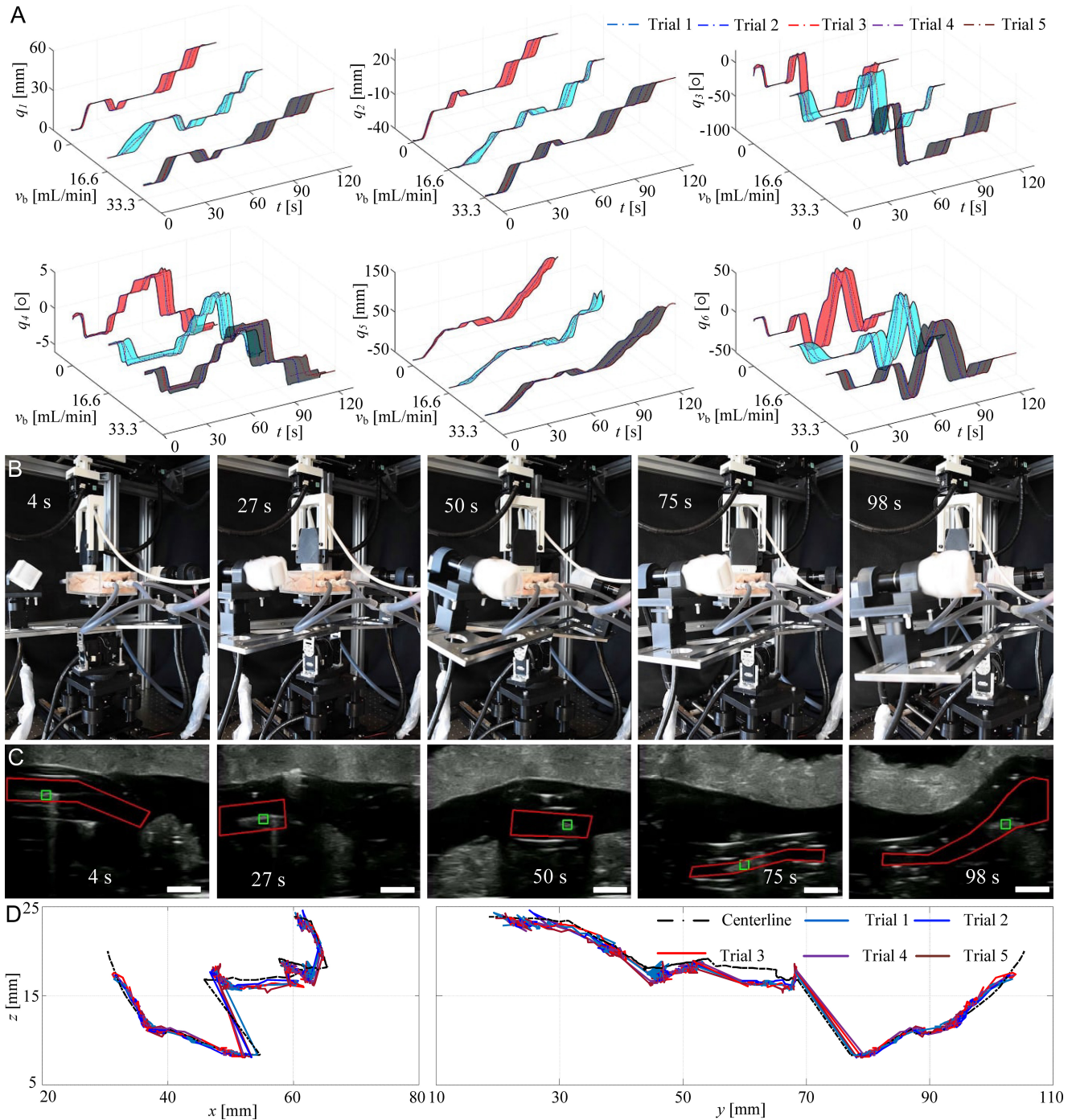


Fig. 5. The USHD is controlled inside path 1 of the 3-D vascular model. (A) Under blood flow rate (v_b) of 0 mL/min, 16.6 mL/min, and 33.3 mL/min, control input of the PMR system can be obtained using the proposed control method when the USHD swims toward target point 1 ($n=5$). (B) During the navigation in path 1, the PMR system is configured at five time instants when the blood flow rate is 16.6 mL/min. (C) For $v_b = 16.6$ mL/min, the 2-D ultrasound images are used to track the USHD in different positions during the closed-loop control experiments. (D) In path 1, the USHD swims toward target point 1 under ultrasound guidance when the blood flow rate is 16.6 mL/min ($n=5$). The scale bar is 5 mm. Please refer to the video S1, Supporting Information.

IV. DISCUSSION

In this paper, we investigate the motion control of a USHD driven by rotating magnetic fields inside a 3-D vascular model. The use of such USHDs holds great promise for minimally invasive procedures in the field of interventional medicine [35]. One of the major advantages of the helical body is its ability to navigate through tortuous blood vessels. The helical

shape allows the USHD to propel itself forward by utilizing the principle of helical motion. By controlling the rotation and translation of the USHD using rotating magnetic fields, precise and controlled movements can be achieved inside the 3-D vascular network. This capability facilitates the targeted delivery of therapeutic agents, such as drug-loaded nanoparticles, to specific regions. However, there are still many factors

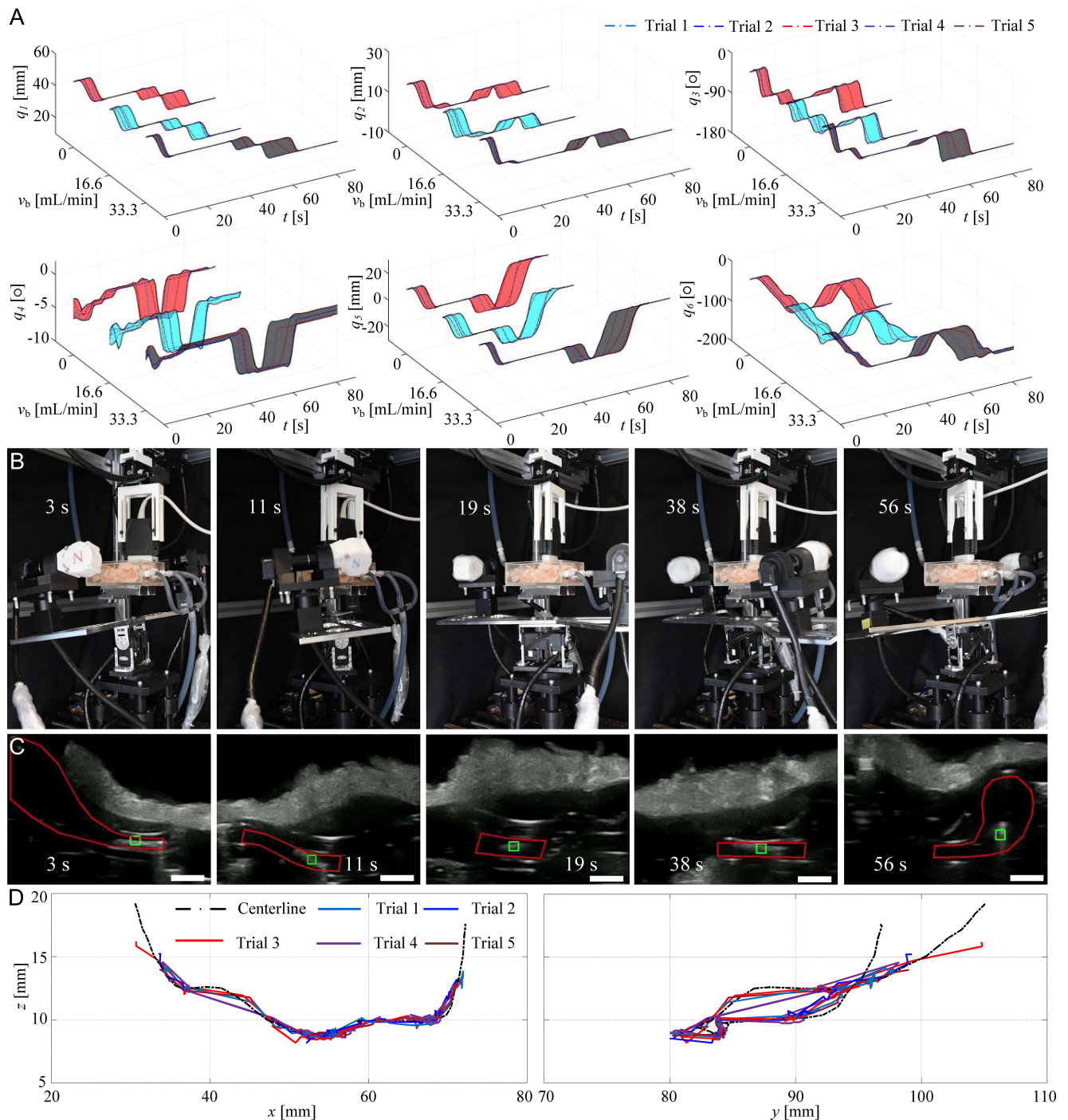


Fig. 6. The USHD is controlled inside path 2 of the 3-D vascular model. (A) Under blood flow rate (v_b) of 0 mL/min, 16.6 mL/min, and 33.3 mL/min, control input of the PMR system can be obtained using the proposed control method when the USHD swims toward target point 2 ($n=5$). (B) During the navigation in path 2, the PMR system is configured at five time instants when the blood flow rate is 16.6 mL/min. (C) For $v_b = 16.6$ mL/min, the 2-D ultrasound images are used to track the USHD in different positions during the closed-loop control experiments. (D) In path 2, the USHD swims toward target point 2 under ultrasound guidance when the blood flow rate is 16.6 mL/min ($n=5$). The scale bar is 5 mm. Please refer to the video S1, Supporting Information.

that must be considered if this technology is to be successfully transferred to the clinic. First, there is room for further improvement in the choice of materials for the USHD. The utilization of soft and biocompatible materials, such as hydrogels, can be advantageous in minimizing tissue impact and reducing potential toxicity associated with the USHD's presence. Second, it is imperative to assess the size of the USHD to prevent potential blockages, as the diameter of the blood vessel

is variable and uncertain. Therefore, careful consideration should be given to the USHD's dimensions to ensure unobstructed passage through these narrow and delicate vessels, minimizing the risk of complications. Thirdly, the stability of the system and the robustness of the proposed control method are crucial for clinical operations. It can be seen from our experiments that when the flow rate increases, the success rate of the experiment decreases. Developing more advanced

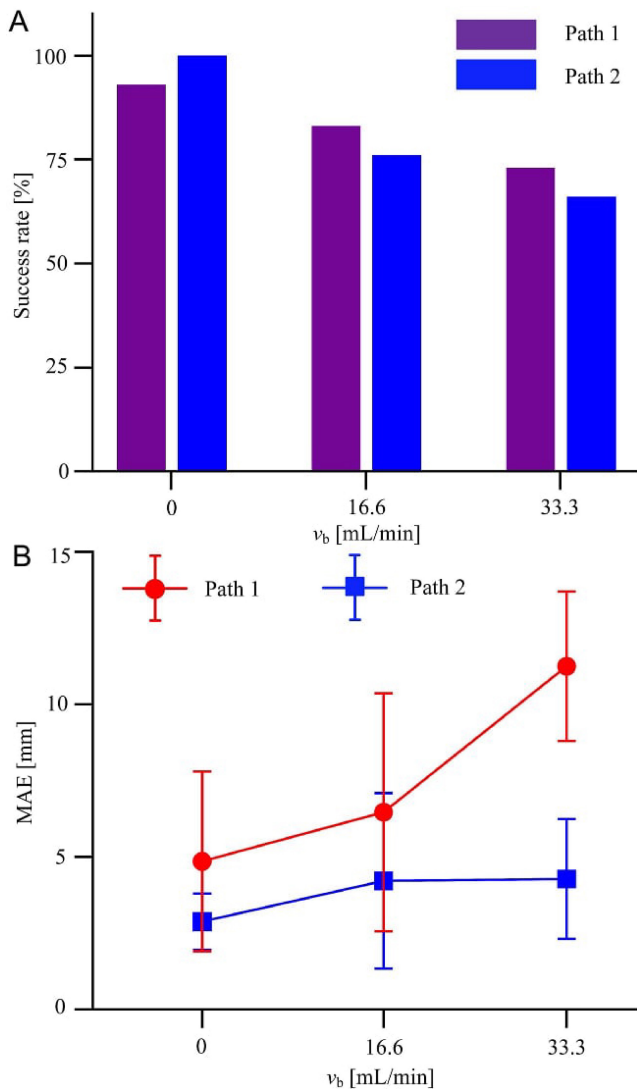


Fig. 7. The USHD is controlled inside paths 1 and 2, when blood flow rates (v_b) are 0 mL/min, 16.6 mL/min, and 33.3 mL/min, respectively. (A) The success rate can be calculated from the 30 consecutive trials ($n=30$) for the different paths and different flow rates. (B) The mean absolute error can be calculated from successful trials under different paths and different flow rates.

and smarter navigation and control mechanisms is crucial to ensure the USHD can effectively maneuver through the complex and dynamic vascular network. Integration of sensing technologies, imaging guidance, and advanced control algorithms may be necessary to enable accurate and real-time navigation. Lastly, in our current PMR system, the separation between the two permanent magnets measures 35 cm. We recognize that this operational space falls short of meeting the demands of real clinical applications. One potential enhancement is to increase the distance between the two permanent magnets, thereby obtaining a larger operational area. Additionally, we are exploring the utilization of permanent magnets with higher magnetic moments to further enhance system performance. These improvements are anticipated to provide our PMR system with a broader range of operation, better aligning with the demands of clinical applications.

During the navigation of the USHD, ultrasound imaging is widely used in conjunction with the USHD for real-time visualization and guidance [25], [36], [37]. It provides valuable information about the blood vessel anatomy, including vessel diameter, tortuosity, and potential obstacles. Furthermore, the measurement of blood flow velocity using the ultrasound imaging system plays a crucial role in the context of the USHD's navigation inside blood vessels. The flow velocity of blood can significantly influence the motion of the USHD. By incorporating real-time blood flow velocity measurements, the USHD can adapt its navigation and motion control strategies accordingly. For instance, high blood flow velocity areas may require the USHD to adjust its speed and propulsion force by changing the frequency of the rotating magnetic field to ensure stable and precise movement. By integrating ultrasound-based flow velocity feedback into the control algorithm, the USHD can optimize its trajectory planning and motion control to effectively maneuver through varying flow conditions. This integration may enable the USHD to navigate more safely and efficiently, improving its overall performance and reducing the risk of potential complications during intravascular procedures. Additionally, in our experiments, the alignment between the USHD's trajectory and the reconstructed path is also influenced by the diameter of the vascular model. The maximum inside diameter of the vascular model we used is approximately 4 mm. In such cases, we ensure precise alignment between the ultrasound probe's position and the reconstructed path, which allows the ultrasound system to effectively detect and navigate the USHD. However, it's worth noting that our proposed approach might encounter challenges in larger blood vessels. The potential for losing control arises due to disparities between the USHD's movement trajectory and the reconstructed path inside these wider vessels.

In actual clinical surgeries, achieving successful navigation of USHD to the targeted pathological region inside blood vessels relies on the prerequisite of 3-D vascular reconstruction. In our experiments, the reconstruction error of the vascular model reaches the millimeter level, which is larger compared to previous state-of-the-art approaches [38], [39], [40] where errors are in the sub-millimeter range. The likely reason behind this is that our segmentation method is not sufficiently accurate. Additionally, our vascular model is flexible, and even minor displacements during the reconstruction process may introduce errors. Further, for real blood vessels in the body, the presence of other tissues and surrounding vessels may impact the accurate reconstruction of the target vessel. Therefore, the combination of advanced medical image segmentation methods [40], [41], [42] becomes crucial to improve the accuracy of the vascular reconstruction. Once the vascular reconstruction is ensured, ROIs pertaining to the vessel can be established, consequently reducing the influence of noise from surrounding structures on tracking of the USHD.

Overall, our study demonstrates the potential of USHDs controlled by rotating magnetic fields for intravascular procedures. The combination of magnetic control, ultrasound

imaging, and motion control strategies provides a promising platform for navigating and performing interventions inside blood vessels.

V. CONCLUSION AND FUTURE WORK

This study demonstrates the successful control of a USHD inside a 3-D vascular model using a PMR system under ultrasound guidance. Before the closed-loop control of the USHD, the centerline of the 3-D vascular model is accurately determined based on 2-D ultrasound images and the position of the ultrasound probe, providing precise waypoints for the USHD. By employing ultrasound guidance, motion control of the USHD is achieved at various blood flow rates. The proposed method enables the determination of joint space coordinates of the PMR system. Analysis of these coordinates reveals that the USHD can be accurately guided to reach the target position within a certain range of control input. These results highlight the effectiveness and robustness of our system in navigating the USHD through a complex vascular network model.

As part of future studies, a biodegradable USHD will be considered, and then we will use the USHD to perform thrombus removal experiments and targeted drug delivery experiments inside the 3-D vascular model under ultrasound imaging guidance. Furthermore, sensor faults will be considered in the closed-loop control experiments of the USHD, and a fault-tolerant control method based on sensor faults will be studied. In addition, we also plan to combine ultrasound images to perform *ex vivo* experiments to verify our PMR system in a time-varying fluid flow rate environment.

REFERENCES

- [1] B. J. Nelson, S. Gervasoni, P. W. Y. Chiu, L. Zhang, and A. Zemmar, "Magnetically actuated medical robots: An *in vivo* perspective," *Proc. IEEE*, vol. 110, no. 7, pp. 1028–1037, Jul. 2022.
- [2] Z. Hosseindoust, B. Mostaghaci, O. Yasa, B.-W. Park, A. V. Singh, and M. Sitti, "Bioengineered and biohybrid bacteria-based systems for drug delivery," *Adv. Drug Del. Rev.*, vol. 106, pp. 27–44, Nov. 2016.
- [3] M. Calik et al., "The measurement of both carotid intima-media thickness and epicardial adipose tissue thickness in children with epilepsy receiving antiepileptic drug therapy," *Epilepsy Behav.*, vol. 85, pp. 110–114, Aug. 2018.
- [4] J. S. Catapano et al., "Subclavian artery to internal carotid artery interpositional bypass for carotid artery occlusion: Technical case report," *Oper. Neurosurg.*, vol. 20, no. 1, pp. E66–E71, 2020.
- [5] E. Bae and T. D. Vo, "Carotid artery angioplasty and stenting for atherosclerotic plaque with mobile intimal flap," *Ann. Vas. Surg.*, vol. 49, pp. e1–e3, May 2018.
- [6] M. Zhang, L. Yang, C. Zhang, Z. Yang, and L. Zhang, "A 5-D large-workspace magnetic localization and actuation system based on an eye-in-hand magnetic sensor array and mobile coils," *IEEE Trans. Instrum. Meas.*, vol. 72, pp. 1–11, 2023.
- [7] L. Yang, M. Zhang, Z. Yang, and L. Zhang, "Multimode control of a parallel-mobile-coil system for adaptable large-workspace micro-robotic actuation," *IEEE/ASME Trans. Mechatronics*, vol. 28, no. 3, pp. 1662–1673, Jun. 2023.
- [8] C. Li, S. Misra, and I. S. M. Khalil, "Closed-loop control characterization of untethered small-scale helical device in physiological fluid with dynamic flow rates," *Adv. Intell. Syst.*, vol. 5, no. 5, 2022, Art. no. 2200322.
- [9] M. Sitti et al., "Biomedical applications of untethered mobile milli/microbots," *Proc. IEEE*, vol. 103, no. 2, pp. 205–224, Feb. 2015.
- [10] M. Cai et al., "Deep reinforcement learning framework-based flow rate rejection control of soft magnetic miniature robots," *IEEE Trans. Cybern.*, early access, Sep. 7, 2022, doi: [10.1109/TCYB.2022.3199213](https://doi.org/10.1109/TCYB.2022.3199213).
- [11] Y. Lu, H. Zhao, A. T. Becker, and J. Leclerc, "Steering rotating magnetic swimmers in 2.5 dimensions using only 2D ultrasonography for position sensing," *IEEE Robot. Autom. Lett.*, vol. 7, no. 2, pp. 3162–3169, Apr. 2022.
- [12] C. Li, F. R. Halfwerk, J. Arens, S. Misra, M. Warlé, and I. S. M. Khalil, "Controlled helical propulsion against the flow of a physiological fluid," in *Proc. IEEE Int. Conf. Manipulation Autom. Robot. Small Scales (MARSS)*, 2022, pp. 1–6.
- [13] J. Sa et al., "Separable and recombinable magnetic robot for robotic endovascular intervention," *IEEE Robot. Autom. Lett.*, vol. 8, no. 4, pp. 1881–1888, Apr. 2023.
- [14] P. E. Dupont et al., "A decade retrospective of medical robotics research from 2010 to 2020," *Sci. Robot.*, vol. 6, no. 60, 2021, Art. no. eabi8017.
- [15] A. W. Mahoney and J. J. Abbott, "Generating rotating magnetic fields with a single permanent magnet for propulsion of untethered magnetic devices in a lumen," *IEEE Trans. Robot.*, vol. 30, no. 2, pp. 411–420, Apr. 2014.
- [16] B. Chaluvadi, K. M. Stewart, A. J. Sperry, H. C. Fu, and J. J. Abbott, "Kinematic model of a magnetic-microbot swarm in a rotating magnetic dipole field," *IEEE Robot. Autom. Lett.*, vol. 5, no. 2, pp. 2419–2426, Apr. 2020.
- [17] M. E. Alshafeei, A. Hosney, A. Klingner, S. Misra, and I. S. M. Khalil, "Magnetic-based motion control of a helical robot using two synchronized rotating dipole fields," in *Proc. 5th IEEE RAS/EMBS Int. Conf. Biomed. Robot. Biomechatron.*, 2014, pp. 151–156.
- [18] D. Mahdy et al., "Characterization of helical propulsion inside *in vitro* and *ex vivo* models of a rabbit aorta," in *Proc. 41st Annu. Int. Conf. IEEE Eng. Med. Biol. Soc. (EMBC)*, 2019, pp. 5283–8286.
- [19] L. Tan and D. J. Cappelleri, "Design, fabrication, and characterization of a helical adaptive multi-material MicroRobot (HAMMR)," *IEEE Robot. Autom. Lett.*, vol. 8, no. 3, pp. 1723–1730, Mar. 2023.
- [20] J. Liu, T. Xu, S. X. Yang, and X. Wu, "Navigation and visual feedback control for magnetically driven helical miniature swimmers," *IEEE Trans. Ind. Informat.*, vol. 16, no. 1, pp. 477–487, Jan. 2020.
- [21] I. S. M. Khalil, A. F. Tabak, K. Sadek, D. Mahdy, N. Hamdi, and M. Sitti, "Rubbing against blood clots using helical robots: Modeling and *in vitro* experimental validation," *IEEE Robot. Autom. Lett.*, vol. 2, no. 2, pp. 927–934, Apr. 2017.
- [22] I. S. M. Khalil et al., "Mechanical rubbing of blood clots using helical robots under ultrasound guidance," *IEEE Robot. Autom. Lett.*, vol. 3, no. 2, pp. 1112–1119, Apr. 2018.
- [23] H. Zhao, J. Leclerc, M. Feucht, O. Bailey, and A. T. Becker, "3D path-following using MRAC on a millimeter-scale spiral-type magnetic robot," *IEEE Robot. Autom. Lett.*, vol. 5, no. 2, pp. 1564–1571, Apr. 2020.
- [24] J. Leclerc, H. Zhao, D. Bao, and A. T. Becker, "*In vitro* design investigation of a rotating helical magnetic swimmer for combined 3-D navigation and blood clot removal," *IEEE Trans. Robot.*, vol. 36, no. 3, pp. 975–982, Jun. 2020.
- [25] L. Yang, M. Zhang, Z. Yang, H. Yang, and L. Zhang, "Mobile ultrasound tracking and magnetic control for long-distance endovascular navigation of untethered miniature robots against pulsatile flow," *Adv. Intell. Syst.*, vol. 4, no. 3, 2022, Art. no. 2100144.
- [26] Z. Yang, L. Yang, M. Zhang, Q. Wang, S. C. H. Yu, and L. Zhang, "Magnetic control of a steerable guidewire under ultrasound guidance using mobile electromagnets," *IEEE Robot. Autom. Lett.*, vol. 6, no. 2, pp. 1280–1287, Apr. 2021.
- [27] J. De Ruijter, J. J. Muijsers, F. N. Van de Vosse, M. R. Van Sambeek, and R. G. Lopata, "A generalized approach for automatic 3-D geometry assessment of blood vessels in transverse ultrasound images using convolutional neural networks," *IEEE Trans. Ultrason., Ferroelect., Freq. Control*, vol. 68, no. 11, pp. 3326–3335, Nov. 2021.
- [28] A. Carovac, F. Smajlovic, and D. Junuzovic, "Application of ultrasound in medicine," *Acta Informatica Medica*, vol. 19, no. 3, p. 168, 2011.
- [29] D. Katritsis, L. Kaiktsis, A. Chaniotis, J. Pantos, E. P. Efstathopoulos, and V. Marmarelis, "Wall shear stress: Theoretical considerations and methods of measurement," *Progr. Cardiovascul. Diseases*, vol. 49, no. 5, pp. 307–329, 2007.

- [30] D. Lopes, H. Puga, J. Teixeira, and R. Lima, "Blood flow simulations in patient-specific geometries of the carotid artery: A systematic review," *J. Biomech.*, vol. 111, Oct. 2020, Art. no. 110019.
- [31] X. Hu, Y. Li, J. Li, and H. Chen, "Effects of altered blood flow induced by the muscle pump on thrombosis in a microfluidic venous valve model," *Lab Chip*, vol. 20, no. 14, pp. 2473–2481, 2020.
- [32] R. O. Ameyya, J. K. Sigey, G. M. O. Maloiy, and D. M. Theuri, "Effect of head position angles on the blood flow in the jugular vein of giraffes," *World J. Mech.*, vol. 11 no. 8, pp. 165–175, Aug. 2021.
- [33] T. W. Fountain, P. V. Kailat, and J. J. Abbott, "Wireless control of magnetic helical microrobots using a rotating-permanent-magnet manipulator," in *Proc. IEEE Int. Conf. Robot. Autom.*, 2010, pp. 576–581.
- [34] A. W. Mahoney, D. L. Cowan, K. M. Miller, and J. J. Abbott, "Control of untethered magnetically actuated tools using a rotating permanent MAGNET in any position," in *Proc. IEEE Int. Conf. Robot. Autom.*, 2012, pp. 3375–3380.
- [35] B. J. Nelson, I. K. Kaliakatsos, and J. J. Abbott, "Microrobots for minimally invasive medicine," *Annu. Rev. Biomed. Eng.*, vol. 12, pp. 55–85, Aug. 2010.
- [36] S. Pane, V. Iacovacci, M. H. D. Ansari, and A. Menciassi, "Dynamic tracking of a magnetic micro-roller using ultrasound phase analysis," *Sci. Rep.*, vol. 11, no. 1, 2021, Art. no. 23239.
- [37] S. Pane, G. Faoro, E. Sinibaldi, V. Iacovacci, and A. Menciassi, "Ultrasound acoustic phase analysis enables robotic visual-servoing of magnetic microrobots," *IEEE Trans. Robot.*, vol. 38, no. 3, pp. 1571–1582, Jun. 2022.
- [38] S. Merouche, L. Allard, E. Montagnon, G. Soulez, P. Bigras, and G. Cloutier, "A robotic ultrasound scanner for automatic vessel tracking and three-dimensional reconstruction of b-mode images," *IEEE Trans. Ultrasonics, Ferroelect., Freq. Control*, vol. 63, no. 1, pp. 35–46, Jan. 2016.
- [39] Z. Jiang et al., "Autonomous robotic screening of tubular structures based only on real-time ultrasound imaging feedback," *IEEE Trans. Ind. Electron.*, vol. 69, no. 7, pp. 7064–7075, Jul. 2022.
- [40] G. Faoro, S. Maglio, S. Pane, V. Iacovacci, and A. Menciassi, "An artificial intelligence-aided robotic platform for ultrasound-guided transcarotid revascularization," *IEEE Robot. Autom. Lett.*, vol. 8, no. 4, pp. 2349–2356, Apr. 2023.
- [41] J. Ni, J. Wu, J. Tong, Z. Chen, and J. Zhao, "GC-Net: Global context network for medical image segmentation," *Comput. Methods Progr. Biomed.*, vol. 190, Jul. 2020, Art. no. 105121.
- [42] C. G. Morales, J. Yao, T. Rane, R. Edman, H. Choset, and A. Dubrawski, "Reslicing ultrasound images for data augmentation and vessel reconstruction," in *Proc. IEEE Int. Conf. Robot. Autom. (ICRA)*, 2023, pp. 2710–2716.